

## The small binary asteroid (939) Isberga <sup>☆</sup>



B. Carry <sup>a,b,\*</sup>, A. Matter <sup>c,d</sup>, P. Scheirich <sup>e</sup>, P. Pravec <sup>e</sup>, L. Molnar <sup>f</sup>, S. Mottola <sup>g</sup>, A. Carbognani <sup>m</sup>, E. Jehin <sup>k</sup>, A. Marciniak <sup>l</sup>, R.P. Binzel <sup>i</sup>, F.E. DeMeo <sup>i,j</sup>, M. Birlan <sup>a</sup>, M. Delbo <sup>h</sup>, E. Barbotin <sup>o,p</sup>, R. Behrend <sup>o,n</sup>, M. Bonnardeau <sup>o,p</sup>, F. Colas <sup>a</sup>, P. Farissier <sup>q</sup>, M. Fauvaud <sup>r,s</sup>, S. Fauvaud <sup>r,s</sup>, C. Gillier <sup>q</sup>, M. Gillon <sup>k</sup>, S. Hellmich <sup>g</sup>, R. Hirsch <sup>l</sup>, A. Leroy <sup>o</sup>, J. Manfroid <sup>k</sup>, J. Montier <sup>o</sup>, E. Morelle <sup>o</sup>, F. Richard <sup>s</sup>, K. Sobkowiak <sup>l</sup>, J. Strajnic <sup>o</sup>, F. Vachier <sup>a</sup>

<sup>a</sup>IMCCE, Observatoire de Paris, UPMC Paris-06, Université Lille1, UMR8028 CNRS, 77 Av. Denfert Rochereau, 75014 Paris, France

<sup>b</sup>European Space Astronomy Centre, ESA, P.O. Box 78, 28691 Villanueva de la Cañada, Madrid, Spain

<sup>c</sup>Max Planck Institut für Radioastronomie, Auf dem Hügel, 69, 53121 Bonn, Germany

<sup>d</sup>UJF-Grenoble 1/CNRS-INSU, Institut de Planétologie et d'Astrophysique de Grenoble (IPAG), UMR 5274, Grenoble F-38041, France

<sup>e</sup>Astronomical Institute, Academy of Sciences of the Czech Republic, Fričova 298, CZ-25165 Ondřejov, Czech Republic

<sup>f</sup>Department of Physics and Astronomy, Calvin College, 3201 Burton SE, Grand Rapids, MI 49546, USA

<sup>g</sup>Deutsches Zentrum für Luft- und Raumfahrt (DLR), 12489 Berlin, Germany

<sup>h</sup>UNS-CNRS-Observatoire de la Côte d'Azur, Laboratoire Lagrange, BP 4229 06304 Nice Cedex 04, France

<sup>i</sup>Department of Earth, Atmospheric and Planetary Sciences, MIT, 77 Massachusetts Avenue, Cambridge, MA 02139, USA

<sup>j</sup>Harvard-Smithsonian Center for Astrophysics, 60 Garden Street, MS-16, Cambridge, MA 02138, USA

<sup>k</sup>Institut d'Astrophysique et de Géophysique, Université de Liège, Allée du 6 août 17, B-4000 Liège, Belgium

<sup>l</sup>Astronomical Observatory Institute, Faculty of Physics, A. Mickiewicz University, Stoleczna 36, 60-286 Poznań, Poland

<sup>m</sup>Astronomical Observatory of the Autonomous Region of the Aosta Valley, Loc. Lignan 39, 11020 Nus (Aosta), Italy

<sup>n</sup>Geneva Observatory, 51 Chemin des Maillettes, CH-1290 Sauverny, Switzerland

<sup>o</sup>CdR & CdL Group: Lightcurves of Minor Planets and Variable Stars, Switzerland

<sup>p</sup>Association des Utilisateurs de Détecteurs Électroniques (AUDE), France

<sup>q</sup>Club d'Astronomie de Lyon Ampère (CALA), Place de la Nation, 69120 Vaulx-en-Velin, France

<sup>r</sup>Observatoire du Bois de Bardonnat, 16110 Taponnat, France

<sup>s</sup>Association T60, 14 Avenue Edouard Belin, 31400 Toulouse, France

### ARTICLE INFO

#### Article history:

Received 8 April 2014

Revised 10 October 2014

Accepted 2 November 2014

Available online 18 November 2014

#### Keywords:

Asteroids, dynamics

Satellites of asteroids

Orbit determination

### ABSTRACT

In understanding the composition and internal structure of asteroids, their density is perhaps the most diagnostic quantity. We aim here at characterizing the surface composition, mutual orbit, size, mass, and density of the small main-belt binary asteroid (939) Isberga. For that, we conduct a suite of multi-technique observations, including optical lightcurves over many epochs, near-infrared spectroscopy, and interferometry in the thermal infrared. We develop a simple geometric model of binary systems to analyze the interferometric data in combination with the results of the lightcurve modeling. From spectroscopy, we classify Isberga as a Sq-type asteroid, consistent with the albedo of  $0.14^{+0.09}_{-0.06}$  (all uncertainties are reported as 3- $\sigma$  range) we determine (average albedo of S-types is  $0.197 \pm 0.153$ , see Pravec et al. (Pravec et al. [2012]. *Icarus* 221, 365–387). Lightcurve analysis reveals that the mutual orbit has a period of  $26.6304 \pm 0.0001$  h, is close to circular (eccentricity lower than 0.1), and has pole coordinates within  $7^\circ$  of  $(225^\circ, +86^\circ)$  in Ecliptic J2000, implying a low obliquity of  $1.5^{+6.0}_{-1.5}$  deg. The combined analysis of lightcurves and interferometric data allows us to determine the dimension of the system and we find volume-equivalent diameters of  $12.4^{+2.5}_{-1.2}$  km and  $3.6^{+0.7}_{-0.3}$  km for Isberga and its satellite, circling each other on a 33 km wide orbit. Their density is assumed equal and found to be  $2.91^{+1.72}_{-2.01}$  g cm<sup>-3</sup>, lower than that of the associated ordinary chondrite meteorites, suggesting the presence of some macroporosity, but typical of S-types of the same size range (Carry [2012]. *Planet. Space Sci.* 73, 98–118). The present study is the first direct measurement of the size of a small main-belt binary. Although the interferometric observations of Isberga are at the edge of MIDI capabilities, the method described here is applicable to others suites of instruments (e.g., LBT, ALMA).

© 2014 Elsevier Inc. All rights reserved.

<sup>☆</sup> Based on observations made with ESO telescopes at the La Silla Paranal Observatory under programme ID: 088.C-0770.

\* Corresponding author at: IMCCE, Observatoire de Paris, UPMC Paris-06, Université Lille1, UMR8028 CNRS, 77 Av. Denfert Rochereau, 75014 Paris, France.

E-mail address: [bcarry@imcce.fr](mailto:bcarry@imcce.fr) (B. Carry).

## 1. Introduction

Of the many properties that describe an asteroid, there is perhaps no quantity more fundamental to understand its composition and internal structure than its density. With the exception of the fine-grained dust returned from asteroid (25143) Itokawa by the Hayabusa spacecraft (Nakamura et al., 2011), our knowledge on the mineralogy of asteroids has been derived from remote-sensing photometry and spectroscopy in the visible and near-infrared, radar polarimetry, and comparison with meteorites studied in the laboratory (e.g., Shepard et al., 2008; Vernazza et al., 2010). These observables, however, tell us about surface composition only, which may or may not be reflective of the bulk composition of the body. The bulk density of meteorites spans a wide range, from the low-density ( $\rho \sim 1.6 \text{ g cm}^{-3}$ ) primitive CI carbonaceous chondrite to the dense ( $\rho \sim 7.4 \text{ g cm}^{-3}$ ) Hexahedrite iron meteorites (see, e.g., Consolmagno and Britt, 1998; Consolmagno et al., 2008, for meteorites density measurements). Comparison of asteroid bulk density with meteorite grain density provides a crude, yet useful, tool in the investigation of their bulk composition. This is particularly valuable for taxonomic types devoid of characteristic absorption bands in their spectrum, for which the analog meteorites cannot be ascertained otherwise.

For asteroids with known surface mineralogy and analog meteorite, the density even allows us to make inference on the internal structure of the body. By comparing the grain density of the surface material to the bulk density of the asteroid, we can detect the presence of denser material below the crust, like in the case of (4) Vesta (Russell et al., 2012), or the presence of large voids, called macroporosity, as for the rubble-pile (25143) Itokawa (Fujiwara et al., 2006). A recent comprehensive analysis of volume and mass determinations of about 300 asteroids has revealed clear differences of density and macroporosity among taxonomic types, together with different trends with size and orbital populations (Carry, 2012). This sample is, however, still limited in number and the precision of the majority of these estimates remains cruder than 50% (1- $\sigma$  cutoff).

In our quest for asteroid masses, the study of binary systems has been the most productive method (Carry, 2012). Spacecraft encounters provide the most precise mass determination (at the percent level, e.g., Pätzold et al., 2011), but they will always remain limited to a few objects, while studies of orbit deflections during planetary encounters provide numerous mass estimates with limited precision (often above 50% relative accuracy, see Zielenbach, 2011; Kuchynka and Folkner, 2013, for instance). With more than 200 binary systems known, and more discoveries announced almost monthly, the study of mutual orbits can provide numerous mass determinations. For large separation binaries, where the companion can be imaged and tracked along its orbit (e.g., Merline et al., 1999; Marchis et al., 2005; Descamps et al., 2011; Carry et al., 2011; Vachier et al., 2012, among others), the mass can be determined to a high precision, typically about 10–15% (Carry et al., 2012). For the small binaries, detected and studied by the signature of mutual eclipses and occultations in their lightcurves, the density can be indirectly determined without measuring the absolute size nor mass of the objects (e.g., Pravec et al., 2006, 2012b). This, however, requires to assume the same bulk density for both components (e.g., Scheirich and Pravec, 2009), which may be problematic if these small-sized binaries are formed by rotational breakup (Walsh et al., 2008). The accuracy reached with this method can range from a few percent to 100% depending on each system (Carry, 2012).

We present here a suite of observations of the small main-belt binary asteroid (939) Isberga (orbital elements:  $a = 2.246 \text{ au}$ ,  $e = 0.177$ ,  $i = 2.588^\circ$ ) aiming at determining its surface composition,

mutual orbit, mass, diameter, density, and macroporosity. We describe in Section 2 the different methods of observation we use, we present the analysis of the surface composition of Isberga in Section 3 and of the physical properties of the system in Section 4.

## 2. Observations and data reduction

### 2.1. Optical lightcurves

The binarity of Isberga was reported by Molnar et al. (2008) from optical lightcurves obtained over 6 nights in 2006 at the Calvin-Rehoboth Observatory. The rotation period of the primary and the orbital period for the satellite were determined to  $2.9173 \pm 0.0003 \text{ h}$  and  $26.8 \pm 0.1 \text{ h}$ . We report observations carried out during 2 nights from the 2008/2009 opposition, 43 nights in 2010, 54 nights in 2011, and 2 nights in 2012. We provide a detailed list of all the lightcurves with ancillary information in Table 1. A subset of the lightcurves is plotted in Fig. 1, showing evidences for mutual events.

As many observers acquired lightcurves of Isberga, we do not go here into the specifics of the data reduction and photometry measurements used by each. Standard procedures were used to reduce the data, including bad pixel removal, bias subtraction, and flat-field correction. Aperture photometry was used to measure the relative flux of Isberga with surrounding stars and build its lightcurves. In lightcurve decomposition, the magnitude scale zero points of individual nights (sessions) were taken as free parameters. Their uncertainties were generally less than 0.01 mag and we checked by experimenting with them that they did not add a significant uncertainty in subsequent modeling of the system, and we did not propagate them there.

### 2.2. Near-infrared spectroscopy

To constrain the surface mineralogy, we acquired a near-infrared spectrum of Isberga on 2011, August the 22nd, at a phase angle of  $28^\circ$ , as part of the MIT-Hawaii-IRTF joint campaign for NEO reconnaissance (Binzel et al., 2006). Data from this survey are publicly available at [smass.mit.edu](http://smass.mit.edu). Observations were taken on the 3-meter NASA Infrared Telescope Facility at the Mauna Kea Observatory. We used the instrument SpeX (Rayner et al., 2003), a near-infrared spectrograph in low resolution mode over 0.8 to  $2.5 \mu\text{m}$ .

Isberga was observed near the meridian (airmass  $< 1.3$ ) in two different positions, here denoted A and B, on a  $0.8 \times 15 \text{ arcsec}^2$  slit aligned north-south. Exposure times were 120 s, and we measured 4 A–B pairs. Solar analog stars were observed at similar airmass throughout the night to correct for telluric absorption. We used the same set of solar analogs as the SMASS program (Binzel et al., 2004, 2006) that have been in use for over a decade.

Data reduction and spectral extraction were performed using the Image Reduction and Analysis Facility (IRAF, Tody, 1993) provided by the National Optical Astronomy Observatories (NOAO). Correction in regions with strong telluric absorption was performed in IDL using an atmospheric transmission (ATRAN) model by Lord (1992). More detailed information on the observing and reduction procedures can be found in Rivkin et al. (2004) and DeMeo and Binzel (2008). We present the resulting spectrum of Isberga in Fig. 2.

### 2.3. Mid-infrared interferometry

Mid-infrared interferometry can provide direct measurements of the angular extension of asteroids (Delbo et al., 2009; Matter et al., 2011, 2013). We used the MID-infrared Interferometric

**Table 1**  
Date, duration ( $\varphi$ ), phase angle ( $\alpha$ ), observatory, and observers of each lightcurve used in present study. The observatory code are IAU codes (G98: Calvín–Rehoboth Observatory, 493: Calar Alto 1.2 m telescope, I40: TRAPPIST at La Silla Observatory, J23: Centre Astronomique de La Couyère, 187: Borowiec observatory, 634: Crolles observatory, 586: T60 and T1M at Pic du Midi), except for Far, MBo, StB, and VFa that correspond to the Farigourette, Michel Bonnardeau's (MBCAA), Saint Barthelemy, and Villefagnan observatories.

Date (UT)	$\varphi$ (h)	$\alpha$ (°)	Obs.	Observers	Date (UT)	$\varphi$ (h)	$\alpha$ (°)	Obs.	Observers
2006-02-24 – 09:36	5.3	11.7	G98	Molnar et al.	2011-09-06 – 14:24	6.0	23.8	493	Mottola, Hellmich
2006-02-26 – 14:24	6.8	12.5	G98	Molnar et al.	2011-09-07 – 16:48	6.3	23.3	493	Mottola, Hellmich
2006-02-27 – 16:48	6.0	12.9	G98	Molnar et al.	2011-09-19 – 21:36	0.4	18.0	I40	Jehin et al.
2006-02-28 – 19:12	7.0	13.3	G98	Molnar et al.	2011-09-25 – 12:00	6.4	15.1	G98	Molnar et al.
2006-03-03 – 07:12	4.5	14.2	G98	Molnar et al.	2011-09-26 – 14:24	7.5	14.5	G98	Molnar et al.
2006-03-04 – 09:36	5.1	14.6	G98	Molnar et al.	2011-09-27 – 16:48	6.2	13.9	G98	Molnar et al.
2008-12-31 – 02:24	1.3	6.2	G98	Molnar et al.	2011-09-28 – 19:12	1.9	13.3	G98	Molnar et al.
2009-01-01 – 02:24	1.3	6.7	G98	Molnar et al.	2011-10-02 – 04:48	1.5	11.3	I40	Jehin et al.
2010-03-25 – 12:00	5.2	3.6	G98	Molnar et al.	2011-10-07 – 16:48	2.4	8.1	I40	Jehin et al.
2010-03-28 – 19:12	6.6	2.1	G98	Molnar et al.	2011-10-08 – 19:12	3.7	7.4	I40	Jehin et al.
2010-04-03 – 07:12	6.4	1.5	G98	Molnar et al.	2011-10-09 – 21:36	4.2	6.8	I40	Jehin et al.
2010-04-07 – 16:48	6.6	3.3	G98	Molnar et al.	2011-10-19 – 21:36	4.7	2.3	J23	Montier
2010-04-08 – 19:12	6.9	3.8	G98	Molnar et al.	2011-10-20 – 00:00	8.5	2.3	VFa	Barbotin, Behrend
2010-04-09 – 21:36	7.0	4.4	G98	Molnar et al.	2011-10-20 – 00:00	8.3	2.3	VFa	Barbotin, Behrend
2010-04-12 – 04:48	7.0	5.4	G98	Molnar et al.	2011-10-21 – 02:24	7.5	2.4	Far	Morelle, Behrend
2010-04-13 – 07:12	5.7	6.0	G98	Molnar et al.	2011-10-21 – 02:24	2.9	2.4	I40	Jehin et al.
2010-04-14 – 09:36	6.0	6.5	G98	Molnar et al.	2011-10-22 – 04:48	9.3	2.6	VFa	Barbotin, Behrend
2010-04-16 – 14:24	4.6	7.5	G98	Molnar et al.	2011-10-22 – 04:48	1.5	2.6	J23	Montier
2010-04-18 – 19:12	5.9	8.5	G98	Molnar et al.	2011-10-22 – 04:48	5.8	2.6	187	Marciniak et al.
2010-04-18 – 19:12	2.4	8.5	G98	Molnar et al.	2011-10-22 – 04:48	7.4	2.6	MBo	Bonnardeau
2010-04-23 – 07:12	5.0	10.5	G98	Molnar et al.	2011-10-22 – 04:48	5.0	2.6	634	Farissier
2010-04-23 – 07:12	3.8	10.5	G98	Molnar et al.	2011-10-25 – 12:00	1.3	4.1	493	Mottola, Hellmich
2010-05-04 – 09:36	5.0	15.0	G98	Molnar et al.	2011-10-26 – 14:24	8.5	4.7	493	Mottola, Hellmich
2010-05-05 – 12:00	4.8	15.4	G98	Molnar et al.	2011-10-26 – 14:24	2.6	4.7	493	Mottola, Hellmich
2010-05-07 – 16:48	2.2	16.2	G98	Molnar et al.	2011-10-27 – 16:48	4.0	5.3	I40	Jehin et al.
2010-05-08 – 19:12	4.5	16.6	G98	Molnar et al.	2011-10-28 – 19:12	4.4	5.9	StB	Carbognani
2010-05-09 – 21:36	4.8	17.0	G98	Molnar et al.	2011-11-01 – 02:24	4.9	7.7	StB	Carbognani
2010-05-10 – 00:00	4.3	17.0	G98	Molnar et al.	2011-11-01 – 02:24	8.0	7.7	493	Mottola, Hellmich
2010-05-11 – 02:24	0.5	17.3	G98	Molnar et al.	2011-11-15 – 12:00	5.7	15.1	StB	Carbognani
2010-05-15 – 12:00	3.1	18.7	G98	Molnar et al.	2011-11-15 – 12:00	3.9	15.1	Far	Morelle, Behrend
2010-05-16 – 14:24	0.5	19.0	G98	Molnar et al.	2011-11-16 – 14:24	5.8	15.6	StB	Carbognani
2010-05-17 – 16:48	2.1	19.3	G98	Molnar et al.	2011-11-16 – 14:24	7.1	15.6	Far	Morelle, Behrend
2010-05-19 – 21:36	3.7	19.9	G98	Molnar et al.	2011-11-17 – 16:48	8.0	16.1	Far	Morelle, Behrend
2010-05-20 – 00:00	2.7	19.9	G98	Molnar et al.	2011-11-18 – 19:12	6.1	16.6	StB	Carbognani
2010-05-21 – 02:24	0.4	20.2	G98	Molnar et al.	2011-11-20 – 00:00	5.8	17.1	StB	Carbognani
2010-05-28 – 19:12	2.7	21.9	G98	Molnar et al.	2011-11-22 – 04:48	6.6	18.0	StB	Carbognani
2010-05-29 – 21:36	3.2	22.1	G98	Molnar et al.	2011-11-26 – 14:24	8.7	19.6	586	Fauvaud et al.
2010-05-30 – 00:00	1.4	22.1	G98	Molnar et al.	2011-11-27 – 16:48	5.3	20.0	586	Fauvaud et al.
2010-05-31 – 02:24	1.8	22.4	G98	Molnar et al.	2011-12-01 – 02:24	0.9	21.1	I40	Jehin et al.
2010-06-01 – 02:24	2.6	22.5	G98	Molnar et al.	2011-12-03 – 07:12	2.4	21.8	I40	Jehin et al.
2010-06-02 – 04:48	2.3	22.7	G98	Molnar et al.	2011-12-04 – 09:36	1.2	22.1	I40	Jehin et al.
2010-06-03 – 07:12	2.6	22.9	G98	Molnar et al.	2011-12-11 – 02:24	2.0	23.8	I40	Jehin et al.
2010-06-04 – 09:36	2.4	23.1	G98	Molnar et al.	2011-12-18 – 19:12	5.0	25.3	493	Mottola, Hellmich
2010-06-08 – 19:12	2.3	23.7	G98	Molnar et al.	2011-12-19 – 21:36	5.7	25.4	493	Mottola, Hellmich
2011-08-29 – 21:36	4.6	26.4	493	Mottola, Hellmich	2011-12-20 – 00:00	6.1	25.5	493	Mottola, Hellmich
2011-08-30 – 00:00	5.0	26.4	493	Mottola, Hellmich	2011-12-21 – 02:24	5.7	25.6	493	Mottola, Hellmich
2011-08-31 – 02:24	5.7	26.0	493	Mottola, Hellmich	2011-12-22 – 04:48	6.0	25.8	493	Mottola, Hellmich
2011-09-03 – 07:12	4.6	25.0	493	Mottola, Hellmich	2011-12-23 – 07:12	5.1	25.9	493	Mottola, Hellmich
2011-09-04 – 09:36	3.1	24.6	493	Mottola, Hellmich	2012-01-18 – 19:12	4.6	27.4	586	Vachier, Colas, Lecacheux
2011-09-05 – 12:00	6.2	24.2	493	Mottola, Hellmich	2012-01-20 – 00:00	4.0	27.3	586	Vachier, Colas, Lecacheux

instrument (MIDI) of the Very Large Telescope Interferometer (VLTI), combining two of the 8.2 m Unitary Telescopes, UT1 and UT2, with a baseline separation of 57 m, providing a high angular resolution of  $\frac{\lambda}{2B} \approx 0.02''$  at  $\lambda \approx 10 \mu\text{m}$ , corresponding to about 10 km projected at the distance of Isberga at the time of observation.

MIDI records the interference fringes between two beams of incoming light, which gives access to the complex degree of coherence (or complex visibility) between the beams. This complex visibility is the Fourier transform of the object brightness distribution on the plane of the sky, stacked along the baseline direction and sampled at the spatial frequency  $\mathbf{B}/\lambda$ , where  $\mathbf{B}$  is the baseline vector. In this work, we focused on the correlated flux observable, which is the modulus of the complex visibility.

Fringes on Isberga were acquired at three observing epochs in visitor mode on 2011, October the 6th, and at four observing epochs in service mode on 2011, October the 10th (Table 2),

following the observing procedure of [Leinert et al. \(2004\)](#). The fringes were dispersed using the prism of MIDI, which provides a spectral resolving power of  $\lambda/\Delta\lambda \approx 30$  at  $\lambda = 10 \mu\text{m}$ . One correlated flux measurement, dispersed over the N-band (from 8 to 13  $\mu\text{m}$ ), was obtained for each observing epoch. Our observations also included a photometric and interferometric calibrator star, HD 15396, to determine the atmospheric and instrumental transfer function. Our calibrator was chosen to be angularly unresolved, and to have a minimum angular separation with the source ( $\approx 3^\circ$ ) and a similar airmass (see Table 2).

The correlated flux measurements of (939) Isberga were extracted using the data reduction software package EWS (Expert WorkStation, see [Jaffe \(2004\)](#), for a detailed description). Using the closest calibrator observation in time, calibrated correlated fluxes of (939) Isberga were obtained by multiplying the ratio target/calibrator star raw correlated flux counts by the absolutely calibrated infrared flux of the calibrator (see [Matter et al. \(2011\)](#),

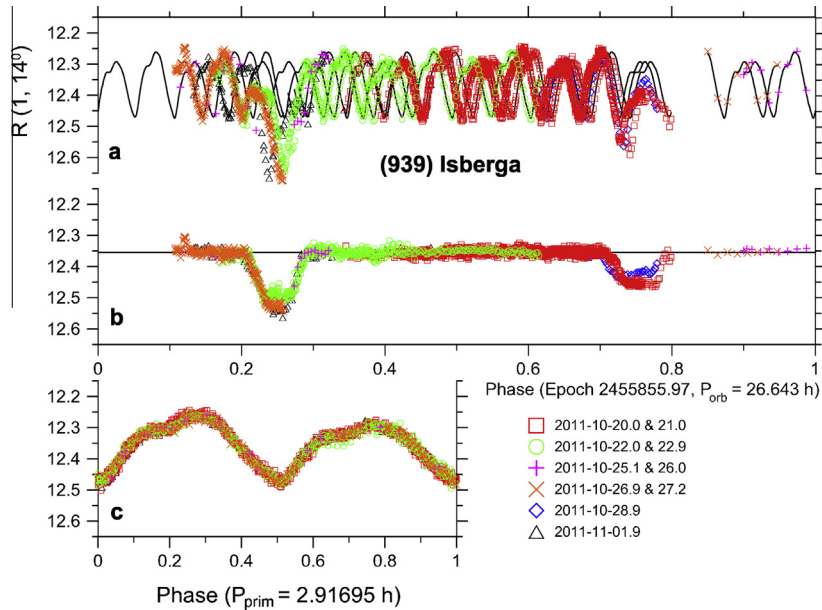


**Fig. 1.** Lightcurves of Isberga showing the mutual eclipses and photometric variability induced by the primary rotation. (a) All the lightcurves acquired between 2011, October the 20th and 2011, November the 1st folded over the synodic orbital period of 26.643 h. (b) The same as above, with the orbital component of the lightcurve only. (c) The rotation component of the lightcurve only, folded over the rotation period of 2.91695 h.

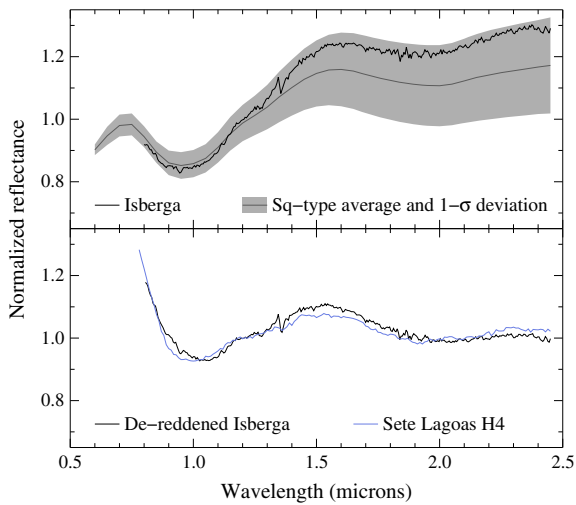


**Fig. 2.** *Top:* Near-infrared spectrum of Isberga normalized at 1.20  $\mu\text{m}$  compared with the average Bus-DeMeo Sq-type spectrum. *Bottom:* De-reddened spectrum of Isberga (using the space weathering model of Brunetto et al., 2006, see Section 3) compared with the ordinary chondrite H4 Sete Lagoas (RELAB sample ID: MH-JFB-021).

2013), for a complete description of the data reduction and calibration procedure).

Uncertainties on the correlated flux are estimated considering two contributions. First, a short timescale effect (much shorter than typical observations of  $\approx 2$  min), dominated by photon noise from the object and thermal background emission. This statistical uncertainty is estimated by splitting a complete exposure, consisting of several thousand of frames and leading to one correlated flux measurement, into five equal parts and by deriving their standard deviation for every spectral channel. Second, the slow variations in the flux transmission of the atmosphere and/or variations of the thermal background can introduce offsets between repeated observations across the night. A rough estimate of this offset-like contribution is obtained by calibrating each correlated flux measurement against all the calibrators of the night, and then computing the standard deviation (see Chesneau, 2007). Such estimate was only possible for the three measurements of 2011, October the 6th where the error bars correspond to the quadratic sum of these two sources of uncertainty.

The four fringe measurements on 2011, October the 10th were acquired over a period of 15 min with only one calibrator observation. Since this is short compared to the estimated rotation and orbital period of Isberga of 2.9 h and 26.8 h respectively, the

**Table 2**

Projected baseline (length  $B$  and position angle  $PA$  counted from north to east), seeing, and airmass for each observation of Isberga and its calibrator (labeled in the last column) using MIDI on the UT1–UT2 baseline of the VLTI.

Object	Date (UT)	$B$ (m)	$PA$ ( $^\circ$ )	Seeing ( $''$ )	Airmass	Label
(939) Isberga	2011-10-07 03:09:43	37.4	14.0	0.53	1.60	1
HD 13596	2011-10-07 03:34:14	37.2	13.0	0.70	1.63	Calib
(939) Isberga	2011-10-07 03:51:45	39.7	21.6	0.76	1.43	2
HD 13596	2011-10-07 04:10:16	39.0	19.8	1.09	1.47	Calib
(939) Isberga	2011-10-07 05:40:04	47.5	33.7	0.72	1.30	3
HD 13596	2011-10-07 06:00:29	46.8	33.1	0.84	1.30	Calib
(939) Isberga	2011-10-10 05:44:02	48.9	34.7	0.70	1.31	4
(939) Isberga	2011-10-10 05:54:27	49.6	35.2	0.70	1.33	4
(939) Isberga	2011-10-10 05:57:56	49.8	35.3	0.70	1.33	4
(939) Isberga	2011-10-10 06:01:53	50.0	35.5	0.76	1.34	4
HD 13596	2011-10-10 06:19:44	49.0	35.0	0.79	1.32	Calib

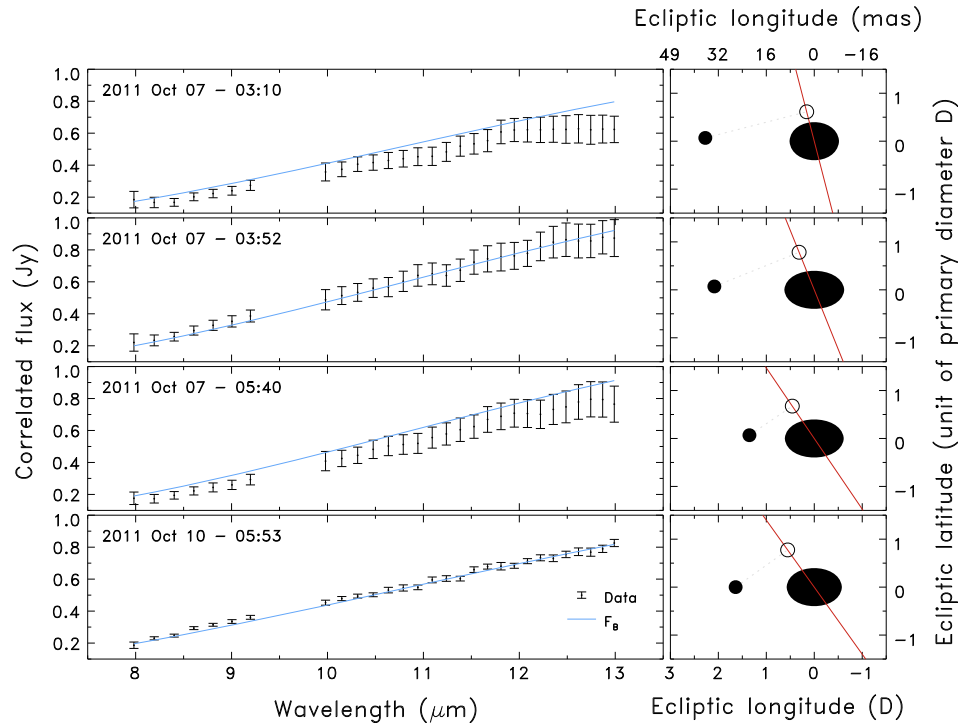


**Fig. 3.** *Left:* Correlated flux of Isberga observed with MIDI over the four epochs listed in Table 2. The best-fit solution of binary model ( $F_B$ ) is also plotted as a solid blue line. *Right:* Corresponding geometry of the system on the plane of the sky. The red line represents the projected VLI baseline, the black ellipse Isberga, the black disk its satellite, and the black circle the projection of the satellite on the baseline. (For interpretation of the references to color in this figure legend, the reader is referred to the web version of this article.)

system apparent geometry, which dominates the data compared to, e.g., putative surface composition heterogeneity, did not change. We thus averaged the four observing epochs to reduce the statistical noise. Assuming that the averaging process also removed the possible offsets affecting the four measurements, the corresponding error bars only include the “averaged” short-term statistical error contribution. Fig. 3 shows the four measurements resulting from the seven initial individual MIDI measurements listed in Table 2.

### 3. Surface composition

We use the Virtual Observatory (VO) service M4AST<sup>1</sup> (Popescu et al., 2012) to analyze the near-infrared reflectance spectrum of Isberga shown in Fig. 2. It presents two broad absorption bands centered at  $0.95 \pm 0.01$  and  $1.91 \pm 0.01$   $\mu\text{m}$ , tracers of olivine and pyroxene assemblages. We classify Isberga as an S- or Sq-type asteroid (in the classification scheme by DeMeo et al. (2009)), the main class in the inner part of the asteroid belt (DeMeo and Carry, 2013, 2014). We also use M4AST to determine the degree of space weathering presented by Isberga’s surface, following the space weathering model by Brunetto et al. (2006), valid for pyroxenes and olivines (see, e.g., Brunetto et al., 2007; Vernazza et al., 2009; Fulvio et al., 2012). In this model, the effect of space weathering is a multiplicative exponential continuum written as  $Ke^{(C_S/2)}$ . This model is based on many laboratory experiments on ordinary chondrites and mimic the effect of space weathering on lunar-like surfaces (increased spectral slope and decreased albedo, see Sasaki et al., 2001; Chapman, 2004; Strazzulla et al., 2005, among others). Space weathering trends are more subtle and complex for asteroids within the S-complex,

**Table 3**

Best-fit values for a circular mutual orbit with 3- $\sigma$  uncertainties of the parameters described in Section 4.1.

Parameter	Value	Unit
$(L_p, B_p)$	(225, +86) <sup>a</sup>	deg.
$P_{orb}$	$26.6304 \pm 0.0001$	h
$L_0$	$354 \pm 3$	deg.
$T_0$	2453790.631170	JD
$e$	$\leq 0.10^b$	
$\omega$	0–360	deg.
$\dot{\omega}$	0–10	deg.
$a/D_{1,C}$	$2.5^{+0.3}_{-0.6}$	
$D_{2,C}/D_{1,C}$	$0.29 \pm 0.02$	
$P_{rot}$	$2.91695 \pm 0.00010$	h
$A_1/C_1$	$1.3^{+0.7}_{-0.07}$	
$A_2/C_2$	1.1 <sup>c</sup>	

<sup>a</sup> The 3- $\sigma$  area is approximately an ellipse of semi-major axes of 8° and 6°, centered on these coordinates, see Fig. 4.

<sup>b</sup> We estimated only an upper limit on the eccentricity from 2011 data.

<sup>c</sup> This is only a formal best-fit value of the elongation of the secondary, a spherical shape is consistent as well.

owing to the different compositions it encompass (Gaffey et al., 1993; Gaffey, 2010), albeit spectral reddening is consistent.

We determine a reddening strength of  $C_S = -0.6$   $\mu\text{m}$ , a value similar to, e.g., (158) Koronis (measured with M4AST on the near-infrared spectrum by Burbine and Binzel (2002) obtained at a phase angle of 19°) and corresponding to significant weathering (responsible for the higher spectral slope of Isberga compared with the average Sq-class of DeMeo et al. (2009) in Fig. 2). The spectrum of Isberga was however obtained at a large phase angle of 28° (Section 2.2), and part of the reddening may be caused by the observing geometry. Spectral observations of Isberga at visible wavelengths

<sup>1</sup> <http://m4ast.imcce.fr/>.

and small phase angle will help refine its taxonomic classification and state of space weathering.

We determine a visible geometric albedo of  $p_V = 0.14^{+0.09}_{-0.06}$  (Section 4.2) which is lower, yet consistent, than the average albedo of asteroids in the S-complex ( $0.197 \pm 0.153$ , see Pravec et al., 2012a, for values based on WISE mid-infrared surveys) and corresponds to the first quartile of all Bus-DeMeo S-complex asteroids (based on Fig. 6 by Mainzer et al., 2011). We finally search for the best-fit (M4AST  $\chi^2$  match) meteorite in the Relab spectral database to Isberga spectrum, corrected from the reddening (either due to the phase angle or space weathering). Ordinary chondrites provide the most-promising candidates, as to be expected from the Sq-type classification, and the best-match is found for the H4 Sete Lagoas (sample MH-JFB-021).

#### 4. Mutual orbit: size, mass, and density

We describe here the different steps that lead to the determination of the geometric properties of the binary Isberga, e.g., component diameter ratio, semi-major axis of the orbit, absolute size.

##### 4.1. Lightcurve analysis and orbit determination

We model the system using the method described in Scheirich and Pravec (2009), modified to allow for precession of the orbit's pericenter. For the modeling, the optical lightcurves were reduced using the technique described in Pravec et al. (2006). In particular, the rotation-induced lightcurve of the primary was fitted using Fourier series and subtracted from the data. The shapes of the components are modeled as ellipsoids, an oblate spheroid for the primary ( $A_1 = B_1 > C_1$ ) and a prolate spheroid for the secondary ( $A_2 > B_2 = C_2$ ), and approximated by polyhedra with triangular facets, orbiting each other on Keplerian orbits. We assume same albedo and density for both components. This assumption is required to translate the unknown mass and diameter ratio of the components into flux ratio (see Scheirich and Pravec, 2009). Depending on the formation scenario, the satellite's density may however be different from that of the primary: under-dense for ejecta re-accumulation or over-dense for ejected boulder (unlikely here given the sizes of Isberga and its satellite). The secondary is moreover assumed to be spin-orbit locked, its long axis aligned with the centers of the two bodies at the pericenter. Finally, spin vectors of both components are assumed to be colinear with mutual orbit pole.

The total brightness of the system as seen by the observer was computed as a sum of contributions from all visible facets, using a ray-tracing code that checks which facets are occulted by or in shadow from the other component. In modeling the eccentric orbit, a precession of the line of apsides was taken into account. A pericenter drift rate depends on primary's oblateness ( $A_1/C_1$ , see Murray and Dermott, 1999, Eq. 6.249) that is only poorly estimated from the lightcurves (see Table 3), so we fit the pericenter drift rate as an independent parameter ( $\dot{\omega}$ ). Its initial values were stepped in a range from zero to  $30^\circ/\text{day}$ ; this range encompasses all possible values for the flattening and other parameters of the system. To reduce a complexity of the modeling, the upper limit on eccentricity is estimated by fitting data from the best-covered apparition (2011) only.

The fitted parameters are the oblateness of the primary, expressed as its equatorial-to-polar semi-major axes ratio,  $A_1/C_1$ ; an elongation of the secondary, expressed as its equatorial (the largest) to polar (the shortest) semi-major axes ratio,  $A_2/C_2$ ; a ratio between the mean cross-section equivalent diameters of the components of the binary ( $D_{2,c}/D_{1,c}$ ); the pole coordinates of the mutual orbit in ecliptic frame,  $L_p$  and  $B_p$  (Epoch J2000); a relative

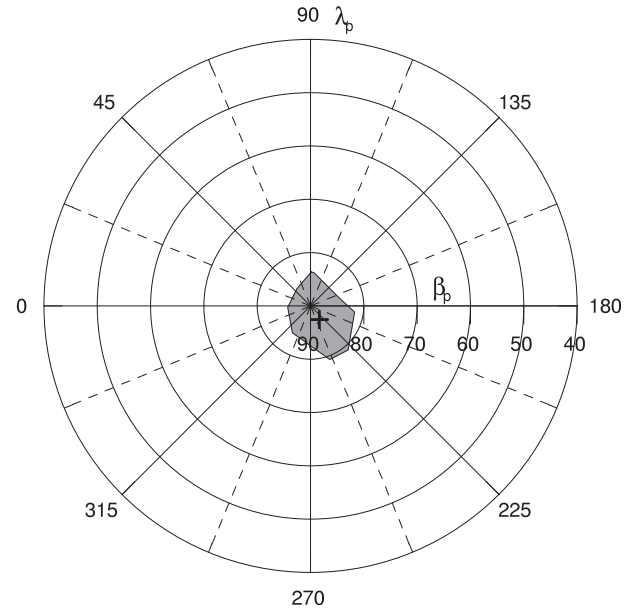


Fig. 4. The  $3\text{-}\sigma$  confidence interval for the pole of the mutual orbit of Isberga (gray area) on an ECJ2000 grid, which can be approximated by an ellipse of semi-major axes of  $8^\circ$  and  $6^\circ$ , respectively. The north pole of the asteroid's heliocentric orbit is marked with the black cross.

size of the mutual orbit's semi-major axis ( $a/D_{1,c}$ ); the mean length  $L_0$  (i.e., the sum of angular distance from the ascending node and the length of the ascending node) for a given epoch  $T_0$ ; the sidereal orbit period  $P_{\text{orb}}$ ; and for modeling the eccentric orbit, the eccentricity  $e$ ; and an argument of pericenter ( $\omega$ ) as well.

We obtain a unique prograde solution of the mutual orbit. The best-fit model parameters are given in Table 3, with uncertainties corresponding to  $3\text{-}\sigma$  confidence level (see Scheirich and Pravec, 2009). The orbital pole coordinates of the system, at a high ecliptic latitude (Fig. 4), implies a small obliquity of  $1.5^{+6.0}_{-1.5}$  deg. Mutual events are therefore constantly observable from Earth, although the geometry remains limited to the equatorial region, precluding a detailed modeling of the 3-D shape of the primary. We constrain the equatorial axes ( $A_1$  and  $B_1$ ) from the amplitude of lightcurves at low phase angle and find  $A_1/B_1 = 1.23 \pm 0.02$ . The oblateness of the primary  $A_1/C_1$  is, however, loosely constrained, with possible values ranging from  $1.2^2$  to 2.0. We do not see any evidence<sup>3</sup> for a strong elongation of the satellite ( $A_2/C_2$ ), even in the long lightcurve observations (6–8 h) that cover a fourth of its rotation period (if it is indeed spin-orbit locked). Examples of the data for the orbital lightcurve component together with the synthetic lightcurve for the best-fit solution are presented in Fig. 5.

##### 4.2. Interferometry analysis and size of the system

To model and interpret the spatial information encoded in the correlated flux, we develop here an extension to the simple model of binary asteroids proposed by Delbo et al. (2009), where the system was described by two uniform disks. Here, we model the primary component of the system by a uniform ellipse, thus taking into account the primary ellipsoid shape and rotation. We denote  $\theta_x$  and  $\theta_y$  (with  $\theta_x > \theta_y$ ) the apparent major axes of the ellipse representing the primary component, and  $\theta_2$  the apparent diameter of the secondary component. The two components are separated by

<sup>2</sup> By definition of the ellipsoid,  $A_1 = B_1 > C_1$ ,  $A_1/C_1$  is thus larger or equal to  $A_1/B_1$ .

<sup>3</sup> The elongation of the secondary is indicated by the amplitude of the long-period component of the lightcurves outside mutual events, which is zero or very low here.

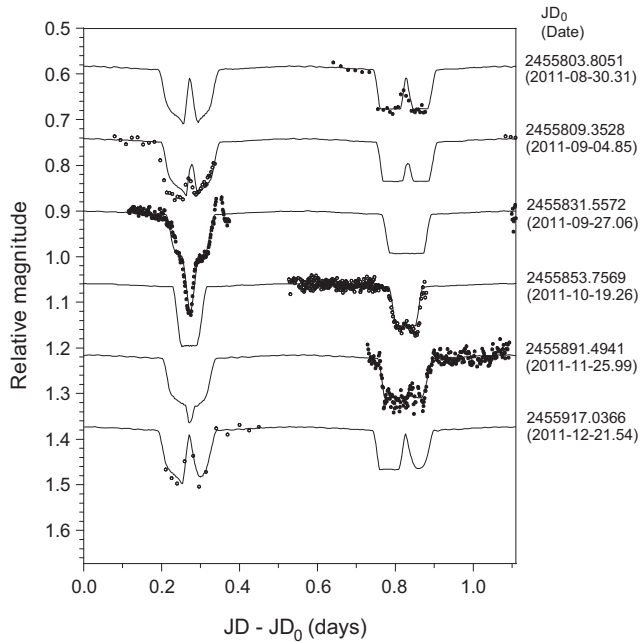


**Fig. 5.** Selected data of the long-period lightcurve component of Isberga during the 2011 apparition, showing the long term evolution. The observed data are marked as points. The solid curve represents the synthetic lightcurve of the best-fit solution.

the angular distance vector  $\mathbf{A}$ . The correlated flux ( $F_B$ ) produced by such a binary system is:

$$F_B(\lambda) = F_1(\lambda, \theta_x, \theta_\beta) \left[ \mathcal{V}_1^{-2}(\lambda) + \mathcal{V}_2^{-2}(\lambda) f_{21}^2 + 2\mathcal{V}_1(\lambda)\mathcal{V}_2(\lambda)f_{21} \cos\left(\frac{2\pi\mathbf{B}}{\lambda} \cdot \mathbf{A}\right) \right]^{\frac{1}{2}} \quad (1)$$

where  $F_1(\lambda, \theta_x, \theta_\beta)$  is the total flux of the first component,  $f_{21} = (\theta_2/\sqrt{\theta_x\theta_\beta})^2$  is the flux ratio between the secondary and primary components,  $\mathbf{B}$  is the baseline vector projected on the plane of the sky, and  $\mathcal{V}_i$  are the intrinsic normalized visibilities<sup>4</sup> of each component  $i$ , computed as

$$\mathcal{V}_i(\lambda) = 2 \frac{J_1(\pi\theta_i \frac{B}{\lambda})}{\pi\theta_i \frac{B}{\lambda}} \quad (2)$$

with  $J_1$  the Bessel function of the first kind of order one, and  $B$  the length of the projected baseline on the plane of the sky. However, a complexity has to be included in the derivation of the visibility expression for the primary component that we assumed to be elliptic and not circular anymore. An ellipse can be seen as a disk that is compressed along one of its axis, thus becoming the semi-minor axis, and then possibly rotated to define the semi-major axis orientation. Therefore, the link between the visibility of a circularly symmetric brightness distribution (uniform disk) and of its inclined and rotated version (ellipse), is obtained by a proper change in the baseline reference frame. This change takes into account a rotation followed by a compression factor along the proper baseline axis (see Berger and Segransan (2007), for more details). This leads to the concept of *effective baseline*:

$$B_{\text{eff}} = \sqrt{B_{u,\gamma}^2 + B_{v,\gamma}^2 \cos\left(\frac{\theta_x}{\theta_\beta}\right)}, \quad (3)$$

<sup>4</sup> The normalized visibility is the ratio between the correlated flux and the total flux.

which is the length of projected baseline expressed in the equatorial reference frame rotated by the angle  $\gamma$ , the position angle, counted from north ( $v$  coordinates) to east ( $u$  coordinates), of the binary separation vector, with

$$B_{u,\gamma} = B_u \cos(\gamma) - B_v \sin(\gamma) \quad (4)$$

$$B_{v,\gamma} = B_u \sin(\gamma) + B_v \cos(\gamma) \quad (5)$$

In this rotated frame, the object recovers a circularly symmetric shape and the visibility expression of the elliptic brightness distribution is thus obtained by replacing, in Eq. (2), the projected baseline length  $B$  (as defined in the initial equatorial reference frame) by the effective baseline length  $B_{\text{eff}}$ , and  $\theta_i$  by the longest axis  $\theta_x$ .

Owing to the low level of the correlated flux of Isberga, we analyze the four epochs together rather than independently, tying all the parameters (4 for each epoch:  $\theta_x$ ,  $\theta_\beta$ ,  $\theta_2$ , and  $A$ ) to the effective, i.e., the cross-section equivalent, diameter of Isberga  $D_C$ . We use the synthetic lightcurve  $m(t)$  of the rotation component (see Section 4.1 and Fig. 1c) to express the apparent major axes of the primary component at each epoch,  $\theta_x(t)$  and  $\theta_\beta(t)$ , as a function of the cross-section equivalent diameter  $D_C$  and the primary oblateness  $A_1/C_1$ . First, assuming that the system is seen equator-on, which is a minor approximation as the latitude of the sub-Earth point is  $4^\circ$  only,  $\theta_\beta(t)$  is constant and equals to the polar dimension  $C_1$ . Second, the lightcurve amplitude provides the ratio of equatorial dimensions  $A_1/B_1 = 10^{-0.4[m_A - m_B]} = 1.23$ , with  $m_A$  and  $m_B$  the minimum and maximum apparent magnitudes over a rotation. With these definitions, we write the cross-section equivalent diameter as:

$$D_C = \sqrt{\langle \theta_x(t) \theta_\beta(t) \rangle} = \sqrt{\langle \theta_x(t) \rangle} C_1, \quad (6)$$

where  $\langle \cdot \rangle$  is the temporal mean over one rotation of the primary. Considering that  $\langle \theta_x(t) \rangle = \sqrt{A_1 B_1}$ , we have:

$$D_C = \sqrt{A_1 \cdot 10^{0.2[m_B - m_A]} C_1} = A_1 \sqrt{\frac{10^{-0.2[m_B - m_A]}}{A_1/C_1}}. \quad (7)$$

Using  $\frac{\theta_x(t)}{A_1} = 10^{-0.4[m(t) - m_A]}$ , we find:

$$\theta_x(t) = D_C \cdot \sqrt{A_1/C_1} \cdot 10^{0.1[m_B - m_A]} \cdot 10^{-0.4[m(t) - m_A]}. \quad (8)$$

With the total flux from the primary  $F_1(\lambda, \theta_x, \theta_\beta)$  evaluated using the NEATM (Harris, 1998), the ratio between the component apparent diameters  $f_{21}$  computed from their physical size ratio of 0.29 (see above, Section 4.1), and the angular separation  $A$  provided by the orbital solution, the free parameters are therefore restricted to the effective diameter  $D_C$  and the oblateness  $A_1/C_1$  of the primary (see Fig. 3 for a representation of the system configuration at each epoch of observation). All other parameters are determined from these two free parameters. The  $\eta$  parameter is considered constant in our NEATM modeling (using the value of  $\eta = 1.211 \pm 0.022$  from Masiero et al., 2011).

We search for the best-fit solution by comparing the correlated flux of the model ( $F_{B,i}$ ), at each epoch  $i$  and for each wavelength  $j$ , with the observations ( $F'_i$ ), for  $D_C$  ranging from 5 to 20 km and  $A_1/C_1$  from 1.2 to 2.0. The goodness of fit indicator we use is

$$\chi^2 = \sum_{i=1}^{N_e} \sum_{j=1}^{N_\lambda} \left( \frac{F_{B,i}(\lambda_j) - F'_i(\lambda_j)}{\sigma_{ij}} \right)^2 \quad (9)$$

where  $N_e$  is the number of epochs,  $N_\lambda$  is the number of correlated flux samples at the epoch  $i$ , and  $\sigma_{ij}$  is the uncertainty on the measured correlated flux. We computed a grid of models by scanning  $D_C$  between 5 and 20 km and  $A_1/C_1$  between 1.2 and 2.0 (see Section 4.1).

As visible in Fig. 6, the  $\chi^2$  statistics is highly peaked around 12 km along the  $D_C$  direction, while it is flatter along the  $A_1/C_1$

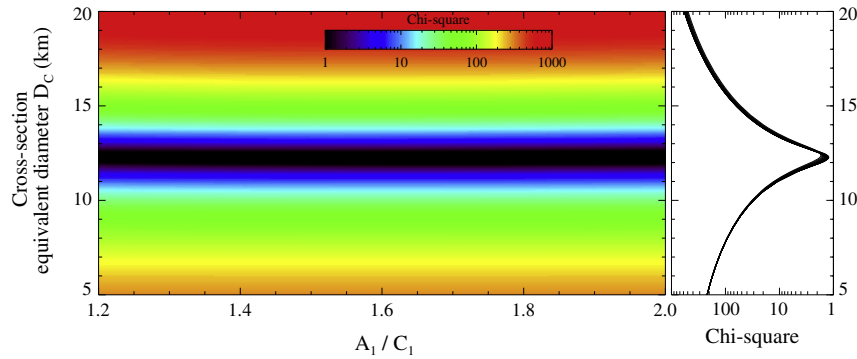


Fig. 6. Goodness of fit for the determination of Isberga effective diameter and oblateness ( $A_1/C_1$ ).

direction. The best-fit to the data is thus obtained for a diameter  $D_c = 12.3 \pm 0.1$  km. Although we cannot estimate accurately the quantitative contribution of the model systematics, we expect them to dominate the uncertainty budget and we adopt a more conservative value of  $D_c = 12.3 \pm 1.2$  km, i.e., a 10% relative accuracy for diameter determination. The low contrast of the  $\chi^2$  statistics does not convincingly restricts the range of 1.2 to 2.0 derived from lightcurves (Section 4.1), although high oblateness seems to be favored by our modeling, with a formal best-fit value of  $A_1/C_1 = 2.00^{+0.00}_{-0.45}$  derived from a Bayesian analysis of the  $\chi^2$  statistics.

We present the best-fit model plotted together with the correlated flux and the system geometry in Fig. 3. Our best-fit solution is in best agreement with the fourth averaged measurement. This is expected given the smaller error bars and thus the stronger weight of this measurement in the fit process. Nevertheless, the best-fit model agrees with the other measurements within their error bars. We can however note a slight discrepancy around 12–13  $\mu\text{m}$  for the first correlated flux measurement.

We use this diameter estimate and the absolute magnitude of  $12.18 \pm 0.27$  we determine following the work by Pravec et al. (2012a) and using observations with Trappist (Table 1) to determine an albedo<sup>5</sup> of  $0.14^{+0.09}_{-0.06}$ . S-type asteroids have higher albedo on average:  $0.197 \pm 0.153$  (Pravec et al., 2012a). Such a value is, however, within the range of possible albedo of S-types.

Masiero et al. (2011) reported a diameter of  $D_W = 10.994 \pm 0.067$  km and an albedo of  $0.21 \pm 0.02$  based on a NEATM (Harris, 1998) analysis of WISE mid-infrared radiometry. Taking into account the binarity of Isberga, this converts into a cross-section equivalent diameter for the primary of  $10.5 \pm 0.1$  km, to be compared with our determination. Considering a 5–10% uncertainty on the diameter determined from WISE to encompass possible systematics (see the comparison of diameter estimates from thermal modeling with other methods in Marchis et al., 2006; Carry, 2012), both determinations converge to a  $\approx 11$  km surface-equivalent diameter for Isberga. The smaller albedo determined here is due to the larger diameter determination.

#### 4.3. Physical properties of Isberga

The results above restrict the primary oblateness  $A_1/C_1$  between 1.2 and 2.0. Because the density determination from the lightcurve analysis is strongly dependent on this parameter, we fix the oblateness between 1.2 and 2.0 by steps of 0.1 and we determine different density values ranging from  $1.89^{+0.85}_{-1.00}$  to  $4.03^{+0.60}_{-1.99}$   $\text{g cm}^{-3}$  ( $3\text{-}\sigma$  confidence interval). Since the ellipsoidal

shape approximation tends to overestimate the volumes of the components, the derived bulk densities should be considered as lower limit estimates. Formally, the  $3\text{-}\sigma$  range for the density is therefore  $2.91^{+1.72}_{-2.01}$   $\text{g cm}^{-3}$ . This level of accuracy corresponds to about 40% relative accuracy at  $1\text{-}\sigma$  level. This crude precision is, however, better than that of 45% of all density determinations (see Fig. 3 in Carry, 2012). This highlights the yet limited knowledge on asteroid interiors.

This density of  $2.91^{+1.72}_{-2.01}$   $\text{g cm}^{-3}$  is very close to the typical density of S-type asteroids at  $2.72 \pm 0.54$   $\text{g cm}^{-3}$  (Carry, 2012). This density is lower than the grain density of the associated H ordinary chondrite meteorites of  $3.72 \pm 0.12$   $\text{g cm}^{-3}$  (Consolmagno et al., 2008). The porosity of Isberga is therefore  $22^{+54}_{-22}\%$ , and its macroporosity can be estimated to  $14^{+66}_{-14}\%$  (using a microporosity of  $7.0 \pm 4.9\%$  on H chondrites measured by Consolmagno et al. (2008)).

The internal structure of Isberga thus encompasses all possible, from compact to highly porous. Although the presence of some macroporosity is likely, better constrains on Isberga polar oblateness are required to conclude. From the current census of S-type densities, and the linear trend of asteroids to range from large

Table 4

Physical characteristics of the binary (939) Isberga. We list the characteristic of the mutual orbit and for both the primary and the satellite their surface- and volume-equivalent diameter, density, and mass. For the primary, we also report the axes ratios and rotation period. Uncertainties are  $3\text{-}\sigma$ . Values of  $A_2/B_2$  and  $A_2/C_2$  are formal best-fit, but values 1.0 are consistent with the data as well.

Parameter	Value	Unit
<i>Primary</i>		
$D_{1,C}$	$12.3 \pm 1.2$	km
$D_{1,V}$	$12.4^{+2.5}_{-1.2}$	km
$\rho_1$	$2.91^{+1.72}_{-2.01}$	$\text{g cm}^{-3}$
$M_1$	$3.52^{+3.90}_{-2.73} \times 10^{15}$	kg
$A_1/B_1$	$1.23 \pm 0.02$	
$A_1/C_1$	$1.3^{+0.7}_{-0.03}$	
$P_{rot}$	$2.91695 \pm 0.00010$	h
<i>Satellite</i>		
$D_{2,C}$	$3.6 \pm 0.5$	km
$D_{2,V}$	$3.6^{+0.7}_{-0.3}$	km
$\rho_2 \equiv \rho_1$	$2.91^{+1.72}_{-2.01}$	$\text{g cm}^{-3}$
$M_2$	$8.60^{+24.1}_{-7.83} \times 10^{13}$	kg
$A_2/B_2$	1.1	
$A_2/C_2$	1.1	
$P_{rot} \equiv P_{orb}$	$26.6304 \pm 0.0001$	h
<i>Mutual orbit</i>		
$a$	$33.0^{+7.6}_{-1.4}$	km
$(i_p, \beta_p)$	$(225, +86) \pm 7$	deg.
$P_{orb}$	$26.6304 \pm 0.0001$	h
$e$	$\leq 0.10$	

<sup>5</sup> We use the widely-used formula between the size  $D$ , the visible absolute magnitude  $H$ , and the geometric visible albedo  $p_v$ :  $D(\text{km}) = 1329p_v^{-1/2}10^{-H/5}$ .

and dense to small and porous (see Fig. 9 in Carry, 2012), it is, however, unlikely that Isberga has a density above  $\approx 3 \text{ g cm}^{-3}$ . We therefore favor solutions with oblateness below 1.5–1.6.

We finally use this density determination to estimate the mass of Isberga and of its satellite: from the primary volume-equivalent diameter  $D_V = \left(\frac{A_1}{C_1}\right)^{-1/6} \left(\frac{A_1}{B_1}\right)^{-1/12} D_C$  (Table 4), we find  $M_1 = 3.52^{+3.90}_{-2.73} \times 10^{15} \text{ kg}$  and  $M_2 = 8.60^{+24.1}_{-7.83} \times 10^{13} \text{ kg}$ , respectively. The size of the Hill sphere associated with these masses is of  $2320^{+650}_{-700}$  and  $670^{+330}_{-370}$  km. The system is therefore extremely compact, the components being separated by only 33 km.

## 5. Conclusion

We present the first mid-infrared interferometric observations of a small binary asteroid, (939) Isberga. Together with low-resolution spectroscopy in the near infrared and an extensive campaign of lightcurves, we conduct a complete characterization of the surface, orbital, and physical properties of the system. It is composed by a 13 km S-type primary and a 4 km secondary, orbiting each other in 26 h on a nearly-circular orbit of semi-major axis 33 km, deep inside the Hill sphere. The inferred density of  $2.91^{+1.72}_{-2.01} \text{ g cm}^{-3}$  is typical for this composition, but the large uncertainties prevent from concluding on the internal structure. The system has a low obliquity ( $1.5^{+6.0}_{-1.5}$  deg.) and mutual eclipses and occultations are always visible from Earth. More lightcurve observations of the system, in particular with absolute photometric reference, will help constrain better the elongation of the secondary and the eccentricity of the mutual orbit.

The low mid-infrared flux of Isberga, at the very edge of VLTI/MIDI capabilities, precludes an independent analysis of these data. The combined analysis of optical lightcurves and mid-infrared visibilities we present here is, however, an efficient way to derive both relative quantities and absolutely scale the system. Among the many small main-belt binaries, all present similar mid-infrared fluxes (given their temperature and apparent angular size), and more sensitive instruments/modes, like the forthcoming VLTI/MATISSE, must be used to better characterize this population of binary systems.

## Acknowledgments

We acknowledge support from the Faculty of the European Space Astronomy Centre (ESAC) for the visits of M. Delbo and A. “Momo” Matter. The work by P.S. and P.P. was supported by the Grant Agency of the Czech Republic, Grant P209/12/0229, and by Program RVO 67985815. A. Matter acknowledges financial support from the Centre National d’Études Spatiales (CNES). TRAPPIST is a project funded by the Belgian Fund for Scientific Research (Fonds National de la Recherche Scientifique, F.R.S.-FNRS) E. Jehin and M. Gillon are FNRS Research Associates, and Jean Manfroid is Research Director of the FNRS. Part of the data utilized in this publication were obtained and made available by the MIT-UH-IRTF Joint Campaign for NEO Reconnaissance. The IRTF is operated by the University of Hawaii under Cooperative Agreement No. NCC 5–538 with the National Aeronautics and Space Administration, Office of Space Science, Planetary Astronomy Program. The MIT component of this work is supported by NASA Grant 09-NEO009–0001, and by the National Science Foundation under Grant Nos. 0506716 and 0907766. F.E.D. acknowledges funding from NASA under Grant No. NNX12AL26G and Hubble Fellowship Grant HST-HF-51319.01-A. Any opinions, findings, and conclusions or recommendations expressed in this material are those of the authors and do not necessarily reflect the views of NASA or the National Science Foundation. This research utilizes spectra

acquired by Jeffery F. Bell with the NASA RELAB facility at Brown University.

## References

- Berger, J.P., Segransan, D., 2007. An introduction to visibility modeling. *New Astron. Rev.* 51, 576–582.
- Binzel, R.P., Rivkin, A.S., Stuart, J.S., Harris, A.W., Bus, S.J., Burbine, T.H., 2004. Observed spectral properties of near-Earth objects: Results for population distribution, source regions, and space weathering processes. *Icarus* 170, 259–294.
- Binzel, R.P., Thomas, C.A., DeMeo, F.E., Tokunaga, A., Rivkin, A.S., Bus, S.J., 2006. The MIT–Hawaii–IRTF joint campaign for NEO spectral reconnaissance. In: Mackwell, S., Stansbery, E. (Eds.), 37th Annual Lunar and Planetary Science Conference. Lunar and Planetary Inst. Technical Report, vol. 37, p. 1491.
- Brunetto, R., de León, J., Licandro, J., 2007. Testing space weathering models on A-type Asteroid (1951) Lick. *Astron. Astrophys.* 472, 653–656.
- Brunetto, R., Vernazza, P., Marchi, S., Birlan, M., Fulchignoni, M., Orfino, V., Strazzulla, G., 2006. Modeling asteroid surfaces from observations and irradiation experiments: The case of 832 Karin. *Icarus* 184, 327–337.
- Burbine, T.H., Binzel, R.P., 2002. Small main-belt asteroid spectroscopic survey in the near-infrared. *Icarus* 159, 468–499.
- Carry, B., 2012. Density of asteroids. *Planet. Space Sci.* 73, 98–118.
- Carry, B. et al., 2011. Integral-field spectroscopy of (90482) Orcus–Vanth. *Astron. Astrophys.* 534, A115.
- Carry, B., Vernazza, P., Dumas, C., Merline, W.J., Mousis, O., Rousselot, P., Jehin, E., Manfroid, J., Fulchignoni, M., Zucconi, J.-M., 2012. The remarkable surface homogeneity of the dawn mission target (1) Ceres. *Icarus* 217, 20–26.
- Chapman, C.R., 2004. Space weathering of asteroid surfaces. *Annu. Rev. Earth Planet. Sci.* 32, 539–567.
- Chesneau, O., 2007. MIDI: Obtaining and analysing interferometric data in the mid-infrared. *New Astron. Rev.* 51, 666–681.
- Consolmagno, G.J., Britt, D.T., 1998. The density and porosity of meteorites from the Vatican collection. *Meteorit. Planet. Sci.* 33, 1231–1241.
- Consolmagno, G., Britt, D., Macke, R., 2008. The significance of meteorite density and porosity. *Chemie der Erde/Geochemistry* 68, 1–29.
- Delbo, M., Liori, S., Matter, A., Cellino, A., Berthier, J., 2009. First VLTI-MIDI direct determinations of asteroid sizes. *Astrophys. J.* 694, 1228–1236.
- DeMeo, F., Binzel, R.P., 2008. Comets in the near-Earth object population. *Icarus* 194, 436–449.
- DeMeo, F., Carry, B., 2013. The taxonomic distribution of asteroids from multi-filter all-sky photometric surveys. *Icarus* 226, 723–741.
- DeMeo, F.E., Carry, B., 2014. Solar System evolution from compositional mapping of the asteroid belt. *Nature* 505, 629–634.
- DeMeo, F.E., Binzel, R.P., Slivan, S.M., Bus, S.J., 2009. An extension of the Bus asteroid taxonomy into the near-infrared. *Icarus* 202, 160–180.
- Descamps, P., Marchis, F., Berthier, J., Emery, J.P., Duchêne, G., de Pater, I., Wong, M.H., Lim, L., Hammel, H.B., Vachier, F., Wiggins, P., Teng-Chuen-Yu, J.-P., Peyrot, A., Pollock, J., Assafin, M., Vieira-Martins, R., Camargo, J.L.B., Braga-Ribas, F., Macomber, B., 2011. Triplexity and physical characteristics of Asteroid (216) Kleopatra. *Icarus* 211, 1022–1033.
- Fujiwara, A. et al., 2006. The rubble-pile Asteroid Itokawa as observed by Hayabusa. *Science* 312, 1330–1334.
- Fulvio, D., Brunetto, R., Vernazza, P., Strazzulla, G., 2012. Space weathering of vesta and v-type asteroids: New irradiation experiments on HED meteorites. *Astron. Astrophys.* 537, L11.
- Gaffey, M.J., 2010. Space weathering and the interpretation of asteroid reflectance spectra. *Icarus* 209, 564–574.
- Gaffey, M.J., Burbine, T.H., Piatek, J.L., Reed, K.L., Chaky, D.A., Bell, J.F., Brown, R.H., 1993. Mineralogical variations within the S-type asteroid class. *Icarus* 106, 573–602.
- Harris, A.W., 1998. A thermal model for near-Earth asteroids. *Icarus* 131, 291–301.
- Jaffe, W.J., 2004. Coherent fringe tracking and visibility estimation for MIDI. In: Traub, W.A. (Ed.), Society of Photo-Optical Instrumentation Engineers (SPIE) Conference Series. Society of Photo-Optical Instrumentation Engineers (SPIE) Conference Series, vol. 5491, p. 715.
- Kuchynka, P., Folkner, W.M., 2013. A new approach to determining asteroid masses from planetary range measurements. *Icarus* 222, 243–253.
- Leinert, C. et al., 2004. Mid-infrared sizes of circumstellar disks around Herbig Ae/Be stars measured with MIDI on the VLTI. *Astron. Astrophys.* 423, 537–548.
- Lord, S.D., 1992. A New Software Tool for Computing Earth’s Atmospheric Transmission of Near- and Far-infrared Radiation. NASA Tech. Mem. (103957).
- Mainzer, A. et al., 2011. NEOWISE studies of spectrophotometrically classified asteroids: Preliminary results. *Astrophys. J.* 741, 90.
- Marchis, F., Descamps, P., Hestroffer, D., Berthier, J., 2005. Discovery of the triple asteroidal system 87 Sylvia. *Nature* 436, 822–824.
- Marchis, F. et al., 2006. Shape, size and multiplicity of main-belt asteroids. *Icarus* 185 (1), 39–63.
- Masiero, J.R. et al., 2011. Main belt asteroids with WISE/NEOWISE. I. Preliminary albedos and diameters. *Astrophys. J.* 741, 68.
- Matter, A., Delbo, M., Liori, S., Crouzet, N., Tanga, P., 2011. Determination of physical properties of the Asteroid (41) Daphne from interferometric observations in the thermal infrared. *Icarus* 215, 47–56.

- Matter, A., Delbo, M., Carry, B., Ligorì, S., 2013. Evidence of a metal-rich surface for the Asteroid (16) Psyche from interferometric observations in the thermal infrared. *Icarus* 226, 419–427.
- Merline, W.J. et al., 1999. Discovery of a Moon orbiting the Asteroid 45 Eugenia. *Nature* 401, 565–568.
- Molnar, L.A., et al., 2008. Lightcurve analysis of a magnitude limited asteroid sample. *Minor Planet Bulletin* 35, 9–12.
- Murray, C.D., Dermott, S.F., 1999. *Solar System Dynamics*. Cambridge University Press.
- Nakamura, T. et al., 2011. Itokawa dust particles: A direct link between S-type asteroids and ordinary chondrites. *Science* 333, 1113–1115.
- Pätzold, M. et al., 2011. Asteroid 21 Lutetia: Low mass, high density. *Science* 334, 491–492.
- Popescu, M., Birhan, M., Nedelcu, D.A., 2012. Modeling of asteroid spectra – M4AST. *Astron. Astrophys.* 544, A130.
- Pravec, P., Scheirich, P., Kušnirák, P., Šarounová, L., Mottola, S., Hahn, G., Brown, P.G., Esquerdo, G.A., Kaiser, N., Krzeminski, Z., Pray, D.P., Warner, B.D., Harris, A.W., Nolan, M.C., Howell, E.S., Benner, L.A.M., Margot, J.-L., Galád, A., Holliday, W., Hicks, M.D., Krugly, Y.N., Tholen, D.J., Whiteley, R.J., Marchis, F., Degraff, D.R., Grauer, A., Larson, S., Velichko, F.P., Cooney, W.R., Stephens, R., Zhu, J., Kirsch, K., Dyvig, R., Snyder, L., Reddy, V., Moore, S., Gajdoš, Š., Világi, J., Masi, G., Higgins, D., Funkhouser, G., Knight, B., Slivan, S.M., Behrend, R., Grenon, M., Burki, G., Roy, R., Demeautis, C., Matter, D., Waelchli, N., Revaz, Y., Klotz, A., Rieugné, M., Thierry, P., Cotrez, V., Brunetto, L., Kober, G., 2006. Photometric survey of binary near-Earth asteroids. *Icarus* 181, 63–93.
- Pravec, P., Harris, A.W., Kušnirák, P., Galád, A., Hornoch, K., 2012a. Absolute magnitudes of asteroids and a revision of asteroid albedo estimates from WISE thermal observations. *Icarus* 221, 365–387.
- Pravec, P., Scheirich, P., Vokrouhlický, D., Harris, A.W., Kušnirák, P., Hornoch, K., Pray, D.P., Higgins, D., Galád, A., Világi, J., Gajdoš, Š., Kornoš, L., Oey, J., Husárik, M., Cooney, W.R., Gross, J., Terrell, D., Durkee, R., Pollock, J., Reichart, D.E., Ivarsen, K., Haislip, J., Lacluyze, A., Krugly, Y.N., Gaftonyuk, N., Stephens, R.D., Dyvig, R., Reddy, V., Chiorny, V., Vaduvescu, O., Longa-Peña, P., Tudorica, A., Warner, B.D., Masi, G., Brinsfield, J., Gonçalves, R., Brown, P., Krzeminski, Z., Gerashchenko, O., Shevchenko, V., Molotov, I., Marchis, F., 2012b. Binary asteroid population. 2. Anisotropic distribution of orbit poles of small, inner main-belt binaries. *Icarus* 218, 125–143.
- Rayner, J.T. et al., 2003. SpeX: A medium-resolution 0.8–5.5 micron spectrograph and imager for the NASA infrared telescope facility. *Publicat. Astron. Soc. Pacific* 115, 362–382.
- Rivkin, A.S., Binzel, R.P., Sunshine, J., Bus, S.J., Burbine, T.H., Saxena, A., 2004. Infrared spectroscopic observations of 69230 Hermes (1937 UB): possible unweathered endmember among ordinary chondrite analogs. *Icarus* 172, 408–414.
- Russell, C.T. et al., 2012. Dawn at Vesta: Testing the protoplanetary paradigm. *Science* 336, 684–686.
- Sasaki, S., Nakamura, K., Hamabe, Y., Kurahashi, E., Hiroi, T., 2001. Production of iron nanoparticles by laser irradiation in a simulation of lunar-like space weathering. *Nature* 410, 555–557.
- Scheirich, P., Pravec, P., 2009. Modeling of lightcurves of binary asteroids. *Icarus* 200, 531–547.
- Shepard, M.K., Clark, B.E., Nolan, M.C., Howell, E.S., Magri, C., Giorgini, J.D., Benner, L.A.M., Ostro, S.J., Harris, A.W., Warner, B.D., Pray, D.P., Pravec, P., Fauerbach, M., Bennett, T., Klotz, A., Behrend, R., Correia, H., Coloma, J., Casulli, S., Rivkin, A.S., 2008. A radar survey of M- and X-class asteroids. *Icarus* 195, 184–205.
- Strazzulla, G., Dotto, E., Binzel, R.P., Brunetto, R., Barucci, M.A., Blanco, A., Orofino, V., 2005. Spectral alteration of the Meteorite Epinal (H5) induced by heavy ion irradiation: A simulation of space weathering effects on near-Earth asteroids. *Icarus* 174, 31–35.
- Tody, D., 1993. IRAF in the nineties. In: Hanisch, R.J., Brissenden, R.J.V., Barnes, J. (Eds.), *Astronomical Data Analysis Software and Systems II*. *Astronomical Society of the Pacific Conference Series*, vol. 52, p. 173.
- Vachier, F., Berthier, J., Marchis, F., 2012. Determination of binary asteroid orbits with a genetic-based algorithm. *Astron. Astrophys.* 543, A68.
- Vernazza, P., Binzel, R.P., Rossi, A., Fulchignoni, M., Birhan, M., 2009. Solar wind as the origin of rapid reddening of asteroid surfaces. *Nature* 458, 993–995.
- Vernazza, P., Carry, B., Emery, J.P., Hora, J.L., Cruikshank, D.P., Binzel, R.P., Jackson, J., Helbert, J., Maturilli, A., 2010. Mid-infrared spectral variability for compositionally similar asteroids: Implications for asteroid particle size distributions. *Icarus* 207, 800–809.
- Walsh, K.J., Richardson, D.C., Michel, P., 2008. Rotational breakup as the origin of small binary asteroids. *Nature* 454, 188–191.
- Zielenbach, W., 2011. Mass determination studies of 104 large asteroids. *Astron. J.* 142, 120–128.